# CIVIL AND ENVIRONMENTAL ENGINEERING REPORTS

# IN-FIELD VERIFICATION OF THE APPLICABILITY OF MEMS-IMU ACCELEROMETERS FOR MONITORING OF MINING-INDUCED SEISMIC ACTIVITY

Lech STOLECKI[1], Krzysztof FUŁAWKA[1*], Thomas FRÜHWIRT[2], Martin SCHIMMEL[3]
[1]KGHM Cuprum R&D, Poland
[2]University of Leoben, Austria
[3]Geociencias Barcelona, GEO3BCN-CSIC, Spain

Abstract

Measurements of seismic activity induced by mining operations are a basic tool for assessing the level of dynamic load associated with the occurrence of tremors. Knowledge of the location of the source of vibrations and the nature of seismicity is the basis for the safe planning of operations and design of both underground and surface infrastructure. The key parameter influencing the quality and reliability of seismic measurements is the coverage density of the analysed area with measurement stations. Unfortunately, the cost of seismic networks using standard devices is so high that in most cases the density of the network is much lower than needed for a good resolution and low event detection threshold. A certain breakthrough in this area may be the introduction of cost-effective measuring devices based on MEMS technology. This study compares the seismic data collected with the use of MEMS-IMU accelerometers with standard accelerometers for field seismic monitoring. The basis for the comparison was the analysis of data recorded by both devices located on the same site for two months. The comparison was carried out in terms of the characteristics of seismic waveforms, their amplitude distribution, frequency characteristics and effective duration of vibrations. Based on the results of the analysis, it was shown that MEMS-IMU accelerometers can be successfully used to monitor seismicity induced by mining activities in the near wave field.

Keywords:    mining-induced seismicity, seismic monitoring, MEMS, accelerometers, dynamic analysis

## 1. INTRODUCTION

Seismicity induced by mining activity generates a threat to surface and underground infrastructures and is burdensome from the point of view of the local community and environment [1,2]. Moreover, in many cases, mining tremors can generate a lethal threat to employees working in underground mines [3-5]. Appropriate monitoring is the basis for determining the genesis of tremors and taking possible actions

---

[1*] Corresponding author: Krzysztof FUŁAWKA, KGHM Cuprum R&D, ul. Gen. Wł. Sikorskiego 2-8, 53-659 Wrocław, krzysztof.fulawka@kghmcuprum.com, +48 71 781 22 45

to reduce the number and intensity of seismic events [6-8]. As experience shows, there are many measuring devices available on the market that provide reliable and continuous measurement of vibrations in both the near and far wave fields. From a practical point of view, an aspect that must be further developed is the increase in the coverage of the analyzed area with measuring devices, which directly affects the accuracy and reliability of the obtained results [9-10]. However, the issue of the high costs related to deployment and maintaining a spatial seismic network remains significant. When using classic seismometers, geophones or accelerometers, expenses are so high that mining operators try to limit the resolution of the seismic network to find the balance between data accuracy and budget limitations. A breakthrough in this area may be the construction of a network using new-generation accelerometers based on Micro-Electro-Mechanical System technology [11-12]. Devices of this type are several to several dozen times cheaper than classic measuring devices, so it is worth checking whether they are useful from the point of view of monitoring of mining-induced seismicity. As part of this study, several months of pilot measurements were carried out using the MEMS-IMU accelerometer (ADIS16470) in the Legnica-Glogow Copper Basin (LGCB) region, which is an area of intense seismic activity induced by underground mining operations. The recorded data were compared with data collected with the use of standard accelerometer SYSCOM-MR3003C in qualitative (general nature of the waveforms) and quantitative manner (dominant frequency values, peak vibration values, effective vibration duration and correlation between the waveforms). The analysis was carried out based on the vibration records generated by high-energy tremors, the source of which was located up to the distance of 5 km from measurement stations.

## 2. DESCRIPTION OF TRIAL SITE

The trial site was the Legnica-Glogow Copper Basin region which is located in southwest Poland. In this area, exploitation is carried out by means of three underground mines, Rudna, Lubin and Polkowice-Sieroszowice (Fig. 1).
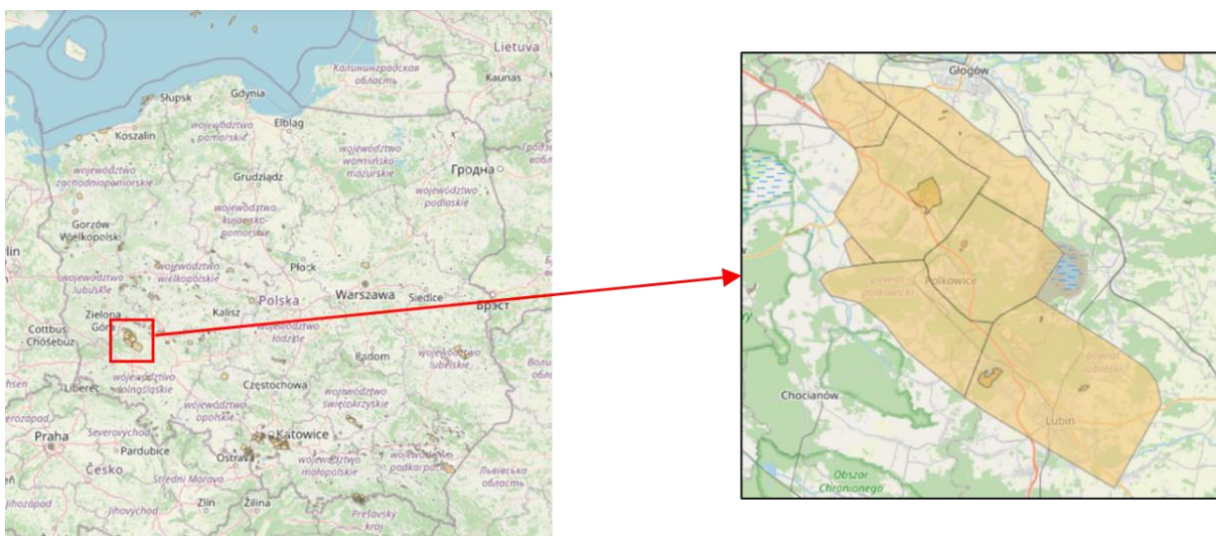


Fig. 1. Location of LGCB mining areas

From a geomechanical point of view, all three mines form one large-area system of underground workings, because they are interconnected. Over sixty years of exploitation, the area of the exploited

deposit has exceeded 500 km$^2$. The deposit is single-level and is located between the Zechstein and Upper Rotliegend formations and lies under a slight inclination towards the NE direction. The depth of the mine ranges from about 700 meters to over 1300 meters below the ground surface (Fig. 2).
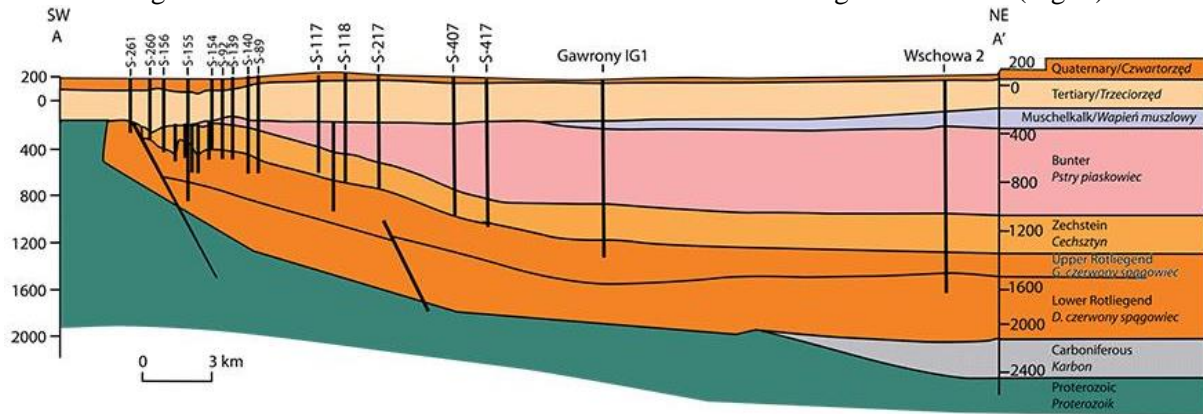


Fig. 2. Geological cross-section through the copper deposits on the Fore-Sudetic Monocline [13]

Unfortunately, given the depth and unfavourable geologic and mining conditions, resulting from the presence of strong rock layers in the roof and weak sandstones within the floor of excavations, exploitation in the LGCB area is accompanied by intense seismic activity. Fig. 3 shows the distribution of the magnitude of mining tremors in the period 12/2013-07/2024.
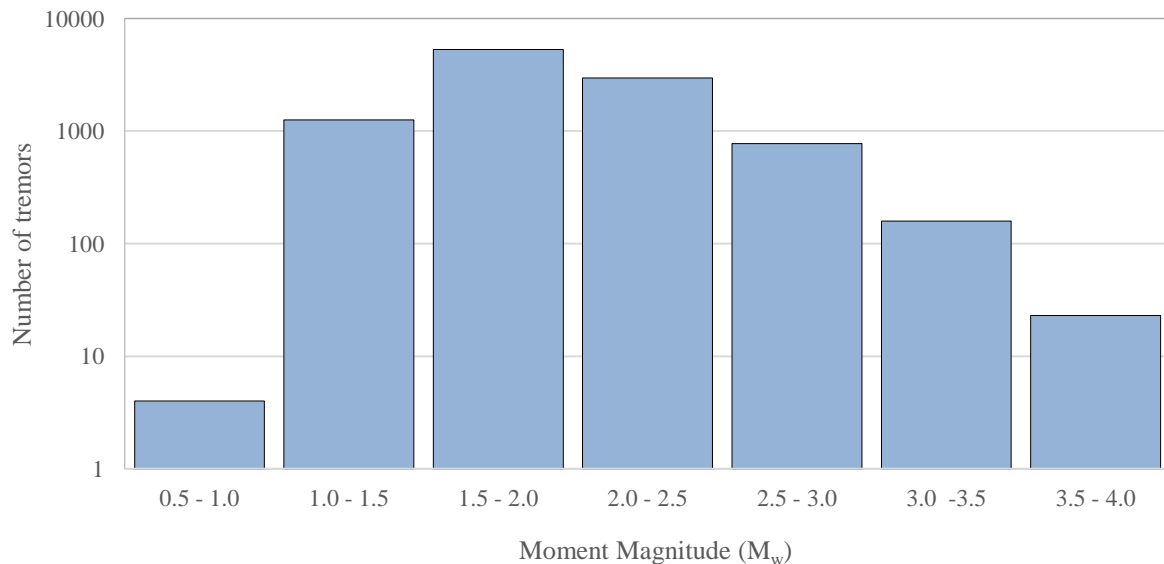


Fig. 3. Magnitude of seismic events in LGCB in the period 12/2013-07/2024
(based on [14])

The location of seismic events in LGCB recorded from 12/2013 concerning seismic devices location is presented in Fig. 4.
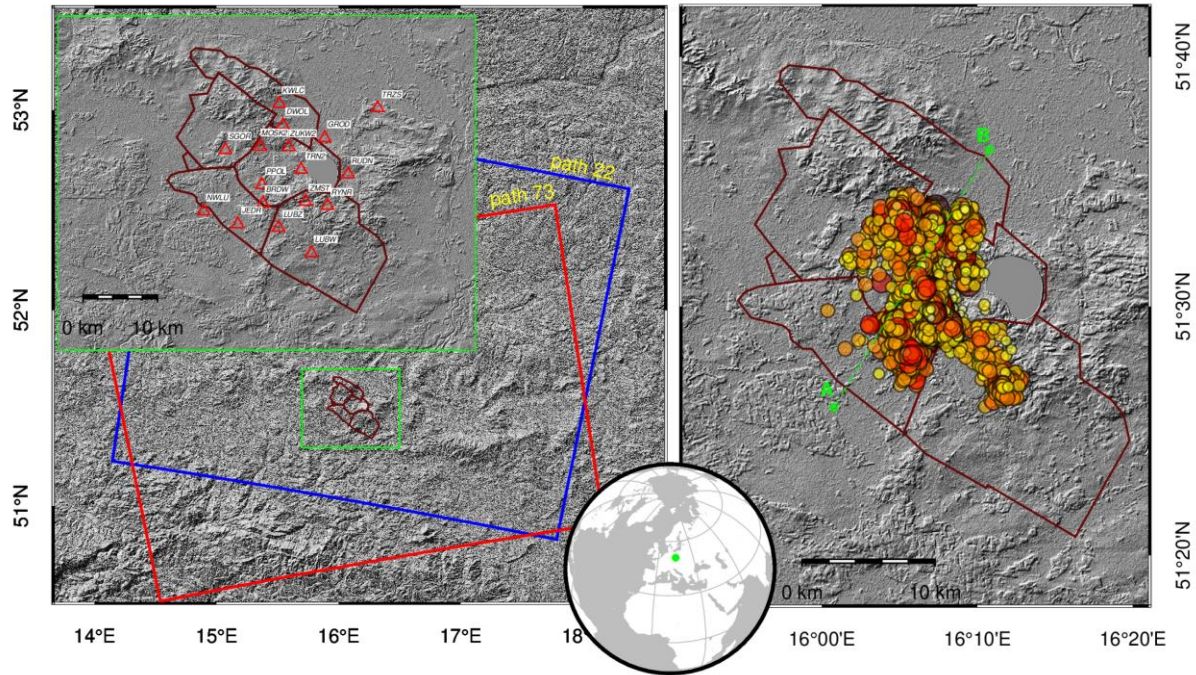
Fig. 4. The location of mining-induced tremors in relation to the KGHM mining areas in the period from 12/2013, and the location of the surface seismic network stations [15]

## 3. MATERIAL AND METHODS

Due to the pilot nature of the induced seismicity measurements using MEMS—IMU (ADIS16470) sensors, an additional classic accelerometer (SYSCOM-MR3003C) was installed in their vicinity for comparison purposes. Data processing and analysis have been performed with us of NI DIAdem software. A detailed description of used devices and signal processing methods has been presented below.

### 3.1. Measuring devices

The ADIS16470 (Fig. 5 - left) is a miniature measurement device based on MEMS-IMU (Microelectromechanical System-Inertial Measurement Unit) technology, containing a three-axis gyroscope and a three-axis accelerometer. The ADIS16470 factory calibration includes each sensor (gyroscope and accelerometer) for sensitivity, bias, stability, and other parameters that determine proper device operation. As a result, each sensor has dynamic compensation formulas that ensure accurate sensor measurements over a wide range of conditions. The ADIS16470 provides a simple, cost-effective method for integrating accurate, multi-axis inertial sensors into industrial systems. All necessary motion testing and calibration are part of the manufacturing process, significantly reducing system build and startup time.

To validate ground vibration records from a low-cost MEMS IMU device, a classic accelerometer SYSCOM MR3003C  was installed in the immediate vicinity of one of the seismic sites for comparative studies (Fig. 5 - right).
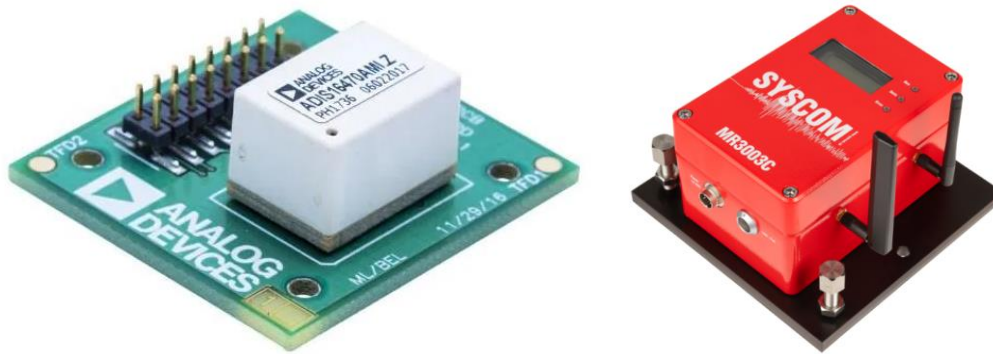
Fig. 5. ADIS16470 accelerometer used for pilot measurements of induced seismicity (left) and three-component measurement system SYSCOM MR3003C for monitoring high-intensity induced seismic vibrations (right)

The technical characteristics of both devices are presented below (Table 1).

Table 1. Basic parameters of the seismic measurement system using the ADIS16470 and MR3003C accelerometers

| Parameter | ADIS16470 | MR3003C |
|---|---|---|
| Resolution | 32 Bit | 24 Bit |
| Number of recording components | 3 components (X,Y,Z) | 3 components (X,Y,Z) |
| Sampling (set up during measurement) | 200 Hz | 250 Hz |
| Measuring range | ±40g | ±4g |
| Housing protection class | - | IP65 |
| Operating temperature range | -25 °C - +85°C | -20 °C - +70°C |
| Battery power supply | - | 14 days |
| Device weight | 0,09 kg | 1.5  kg |

### 3.2. Signal Filtering

Due to the vibration characteristics in the LGCB region, a low-pass filter in the range of <40 Hz was set in the MEMS recording system. Therefore, before starting the calculation all seismic waveforms were filtered in a band consistent with the frequency response of the MEMS measurement system and the frequency response of events recorded. As a result, waveforms recorded with both devices were filtered in the range of 0.1-40 Hz using a fourth-order Butterworth band-pass filter. All signals were subjected to an offset zeroing procedure.

### 3.3. Peak particle acceleration and effective vibration duration

As part of the comparison, the values of the duration of the maximum vibration phase and the values of the maximum horizontal amplitude of vibration acceleration ($PGA_{H10}$) were determined. These parameters are used in seismic scales to assess dynamic impacts on infrastructure located on the surface. The value of the maximum horizontal amplitude of vibration acceleration ($PGA_{H10}$) is determined according to the formula:

$$PGA_{H10} = max\left(\sqrt{a_x^2(t) + a_y^2(t)}\right) \tag{3.1}$$

where: $a_x(t)$ – the magnitude of vibration acceleration recorded on the horizontal component X; $a_y(t)$ – the magnitude of vibration acceleration recorded on the horizontal component Y.

The duration of the maximum phase of the vibration is determined from the integral of the sum of squares of the horizontal acceleration components of the vibration. The duration is the time interval between those moments when the Arias intensity reaches 5% and 95% of its value:

$$I_A(t_k) = \int_0^{t_k} \left( a_X^2(t) + a_Y^2(t) \right) dt \tag{3.2}$$

where: $t_k$ – variable describing the dependence of Arias intensity on time.

For uniform calculation of duration, the normalized Arias intensity graph is used:

$$I_{HA}(t_k) = \frac{\int_0^{t_k} \left( a_X^2(t) + a_Y^2(t) \right) dt}{\int_0^{t_A} \left( a_X^2(t) + a_Y^2(t) \right) dt} \tag{3.3}$$

where: $t_A$ – total duration of vibration acceleration recording.

### 3.4. Seismic noise analysis

To analyze the spectral characteristics of the noise, the Power Spectral Density (PSD) of the signal was calculated. Based on the PSD, the distribution of the signal power concerning frequency changes was estimated. The calculations were performed using the commonly used approach to quantification of seismic noise using the Fourier transform. PSD was calculated according to the formula:

$$PSD = \frac{RMS^2}{\Delta F} \tag{3.4}$$

where: $RMS$ - root mean square of the seismic signal; $\Delta F$ - frequency interval.

This approach is currently the standard technique for quantification of seismic noise, as emphasized in publications [9, 16-17].

### 3.5. Recording rate unification for direct correlation calculations

The difference in the recording frequency of both measurement systems affects the possibility of calculating correlations between individual vibration records. A different number of points determines a situation in which individual intervals of the vibration record adopt a different trend despite the overlap of the curves. The situations are illustrated in Fig. 6. As can be seen, the trend of the course of individual intervals is convergent only in the initial phase of the record (sections 1-2 and 2-3). With time progressing, the discrepancies are more and more visible, which causes the impossibility of calculating correlations between individual courses or their envelopes. This is particularly visible at the points of the curve break, e.g. sections 3-4 or 7-8.
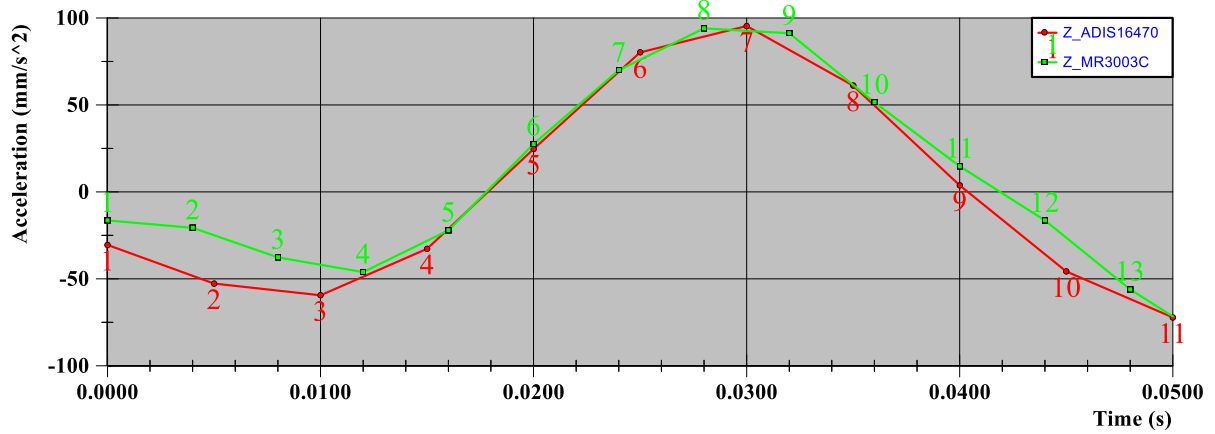
Fig. 6. Comparison of recordings from an IMU system with a sampling rate of 200 Hz (red) and a classic system with a sampling rate of 250 Hz

Therefore, it is necessary to generate waveform that will be characterized by the same number of points and a good fit to the real recordings. For this purpose, spline functions can be used, which allow for the approximation of complex shapes by fitting curves with given intervals. In NI DIAdem software, both parametric and nonparametric splines are built from cubic functions and are twice continuously differentiable at successive points. Unfortunately, splines of this type are not suitable for all data sets, especially for vibration recordings characterized by high randomness of the waveforms. To increase the accuracy of curve fitting, spline functions in the form of subsplines were used, specifically the Akima subsplines method [18]. The Akima subspline is an interpolating function in the form of a piecewise cubic polynomial, similar to the cubic spline:

$$A(x)|_{x \in [x_i, x_{i+1}]} = a_i + b_i(x - x_i) + c_i(x - x_i)^2 + d_i(x - x_i)^3 \doteq A_{i(x)} \tag{3.5}$$

where: $a_i$, $b_i$, $c_i$ and $d_i$ are defined by the value of the derivatives $A_i' \doteq A_{(x_i)}'$ of the subspline through the continuity conditions of the subspline and its first derivative:

$$A_{i(x_i)} = y_i, A_{i(x_i)}' = A_i', A_{i(x_{i+1})} = y_{i+1}, A_{i(x_{i+1})}' = A_{i+1}' \tag{3.6}$$

After substituting (2.5) into (2.6) we get:

$$a_i = y_i, b_i = A_i', c_i \frac{3p_i - 2A_i' - A_{i+1}'}{\Delta x_i}, d_i = \frac{A_i' + A_{i+1}' - 2p_i}{(\Delta x|i)^2} \tag{3.7}$$

where: $p_i \doteq \frac{\Delta y_i}{\Delta x_i}, \Delta y_i \doteq y_{i+1} - y_i, \Delta x_i \doteq x_{i+1} - x_i.$

In an ordinary cubic spline, the derivatives of $A_i'$ are determined by the continuity condition of the second derivative of the spline. Subsplines do without this continuity condition and can instead use the derivatives as arbitrary parameters that can be chosen to satisfy another condition. Akima suggested minimizing the deviations by choosing the derivatives as linear combinations closest to the slopes:

$$A_i' = \frac{w_{i+1}p_{i-1} + w_{i-1}p_i}{w_{i+1} + w_{i-1}}, \text{ if } w_{i+1} + w_{i-1} \neq 0 \tag{3.8}$$

$$A'_i = \frac{p_{i-1}+p_i}{2}, \text{if } w_{i+1} + w_{i-1} = 0 \qquad (3.9)$$

where the weights $w_i$ are defined by the equation:

$$w_i = |p_i - p_{i-1}| \qquad (3.10)$$

It is assumed that if three points lie close to a line, then the subspline in this neighborhood must lie close to this line. In other words, if $|p_i - p_{i-1}|$ is small, the nearby derivatives must be close to $p_i$. Only the first two and the last two points need a special description, e.g. according to:

$$A'_1 = p_1, A'_2 = \frac{1}{2}p_1 + \frac{1}{2}p_2, A'_n = p_{n-1}, A'_{n-1} = \frac{1}{2}p_{n-1} + \frac{1}{2}p_{n-2} \qquad (3.11)$$

The subsplines in the applied method are built from n-th order polynomials and are continuously differentiable only n-2 times. The difference between using standard splines and Akima subsplines is shown in Fig. 7.
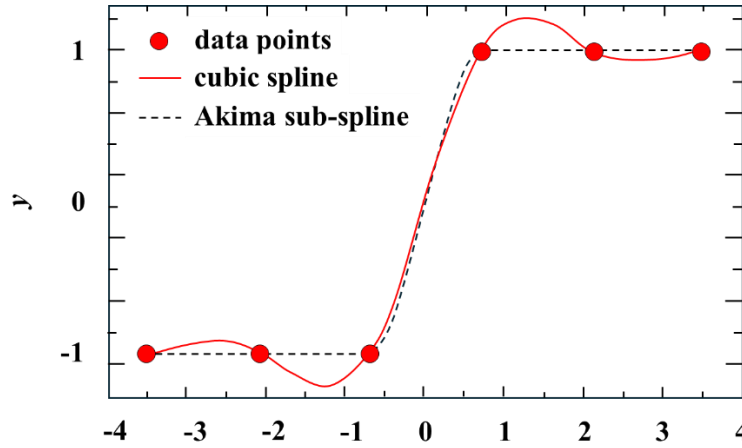


Fig. 7. Cubic spline (solid red line) showing typical deviations compared to Akima subspline (dashed black line) where deviations are removed

As a result, it was possible to generate curves for recordings made with a classic accelerometer with a reduced number of points corresponding to a clock frequency of 200 Hz (Fig. 8).
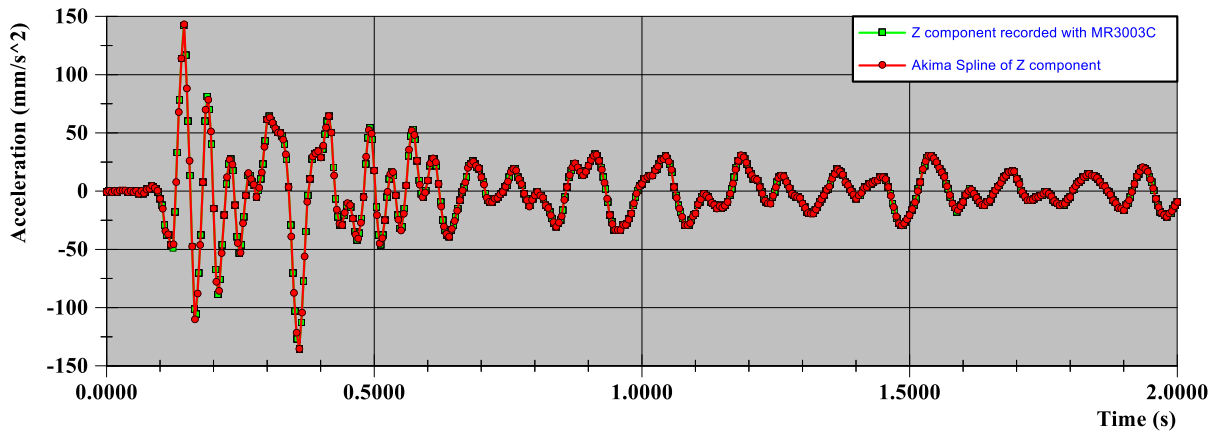


Fig. 8. Example of a curve generated using Akima subsplines (green squares - f = 200 Hz) with respect to real data recorded using the classical system (red circles - f = 250 Hz)

## 4. RESULTS

During the 2 months of continuous measurement, 8 events with a magnitude of $M_w$ 2.0 to $M_w$ 2.5 were recorded. The details of recorded tremors are presented in Table 2.

Table 2. List of analysed high-energy mining tremors

| No. | Date | Time | Energy [J] | Magnitude |
|---|---|---|---|---|
| 1 | 19/09/2023 | 10:10:01 | 5.4E+05 | 2.3 |
| 2 | 22/09/2023 | 19:34:31 | 1.2E+05 | 2.0 |
| 3 | 28/09/2023 | 03:45:28 | 1.7E+05 | 2.1 |
| 4 | 12/10/2023 | 03:01:16 | 2.2E+05 | 2.1 |
| 5 | 13/10/2023 | 14:44:40 | 1.4E+06 | 2.5 |
| 6 | 17/10/2023 | 12:04:51 | 1.7E+05 | 2.1 |
| 7 | 17/11/2023 | 20:38:57 | 2.0E+05 | 2.1 |
| 8 | 18/11/2023 | 03:04:12 | 2.3E+05 | 2.1 |

### 4.1. Peak particle acceleration and effective vibration duration

Reliable information on the amplitude characteristics of vibrations recorded on the surface is essential for the correct determination of the threat to surface infrastructure resulting from seismic activity induced by mining activities. It is important that all seismic devices belonging to one network are calibrated in a way that ensures convergent results under the same seismic conditions. Fig. 9 presents the results of the comparison of peak PGA (Peak Ground Acceleration) vibration acceleration values recorded using both measuring stations. The peak vibration values were determined with respect to the applied infrastructure monitoring standards and seismic intensity scales used in LGCB region. Therefore peak value of acceleration was determined based on the horizontal record (x, y) in the frequency band up to 10 Hz, hence the PGA is designated with the $_{H10}$ index.
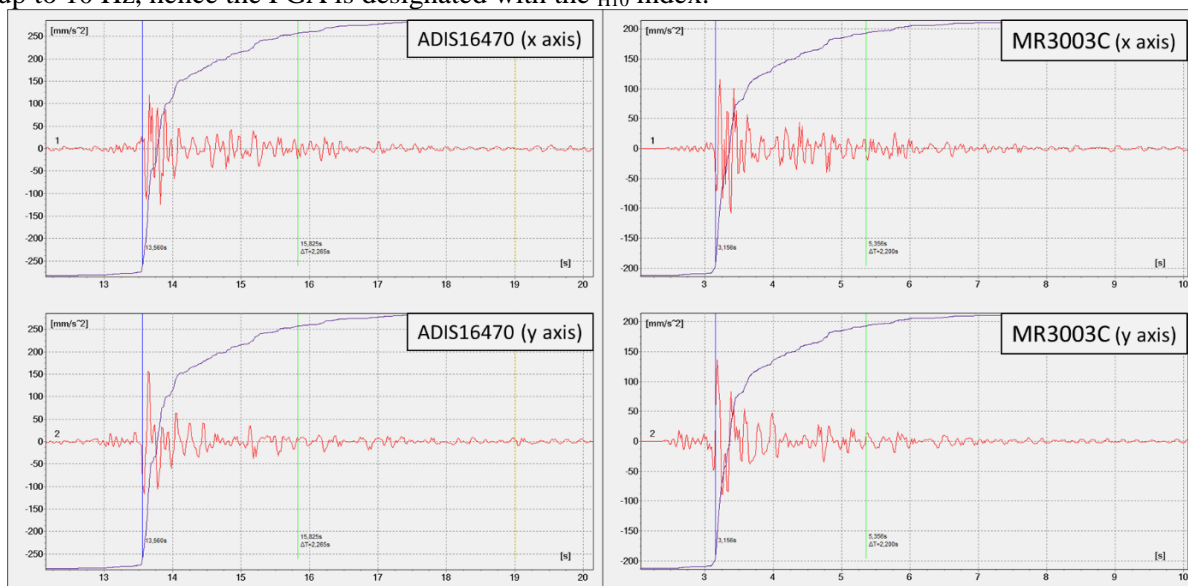


Fig. 9. Duration of the maximum phase of vibrations after a tremor with the energy of $1.4 \times 10^6$ J from 13/10/2023 - ADIS16470(left) and MR3003C (right)

The obtained results prove that the appropriate quality standard of the signal recorded by the IMU accelerometer is maintained. The obtained difference in signal durations did not exceed ±15% of the duration determined from the recording obtained with the classic accelerometer. The maximum difference was 14.7%, which translated into a time difference of 0.5 seconds. On the other hand, the average value for all analyzed recordings was 7.04%. This level of error is permissible in the case of vibration analyses recorded with different measuring devices. Additionally, Table 3. compares the values of the horizontal maximum amplitude of vibration acceleration ($PGA_{H10}$). In these cases, a large match was also obtained between the results obtained with the analyzed measuring devices. The maximum difference was 15.2%, which translated into a difference between the determined accelerations of 4.0 mm/s$^2$. The average value for all analyzed recordings was 10.3 mm/s$^2$. Such small differences between the determined values indicate the appropriate quality of the signal from the IMU - ADIS16470 accelerometer.

Table 3. Summary of the obtained results of the analyses of the duration ($t_{Ha}$) and the maximum horizontal amplitude of vibration acceleration ($PGA_{H10}$)

| No. | Date | ADIS16470 | | MR3003C | | Difference | |
|---|---|---|---|---|---|---|---|
| | | $t_{Ha}$ [s] | $PGA_{H10}$ [mm/s$^2$] | $t_{Ha}$ [s] | $PGA_{H10}$ [mm/s$^2$] | $t_{Ha}$ [%] | $PGA_{H10}$ [%] |
| 1 | 19/09/2023 | 2.8 | 62 | 2.9 | 55 | 3.4 | 12.7 |
| 2 | 22/09/2023 | 4.2 | 20 | 4.3 | 19 | 2.3 | 5.2 |
| 3 | 28/09/2023 | 3.9 | 34 | 3.4 | 30 | 14.7 | 13.3 |
| 4 | 12/10/2023 | 3.5 | 53 | 3.8 | 46 | 7.9 | 15.2 |
| 5 | 13/10/2023 | 2.3 | 160 | 2.2 | 140 | 4.5 | 14.0 |
| 6 | 17/10/2023 | 3.8 | 46 | 3.5 | 40 | 8.6 | 15.0 |
| 7 | 17/11/2023 | 3.5 | 58 | 3.1 | 58 | 12.9 | 0 |
| 8 | 18/11/2023 | 5.2 | 60 | 5.1 | 56 | 2.0 | 7.1 |

## 4.2. Seismic noise analysis

Based on the recorded data and the conducted comparison, it can be stated that the noise recorded using the ADIS16470 accelerometer based on MEMS IMU technology was characterized by a significantly higher level compared to the PSD of the noise recorded with the classic accelerometer, both in the horizontal and vertical direction (Fig. 10). It has to be highlighted that PSD graphs were prepared based on raw data from the recorders, however, Figure 10 shows a clear decrease in PSD after reaching 40 Hz. This is due to the bulit-in filtering of the signal below 40 Hz already at the level of the MEMS system, as described in section 3. Nevertheless, from the point of view of this analysis, the PSD values in the range of 0.1-40 Hz are crucial. In this frequency window, the range of frequencies contained in the noise was much larger. This situation indicates the lower efficiency of the ADIS16470 accelerometer in the scope of observing microseismic phenomena compared to classic accelerometric systems. Relatively high noise levels also complicate the task of determining the epicentral and hypocentral location of the vibration source, due to difficulties in the precise determination of the arrival times of P and S waves. However, based on the pilot recordings and after comparing the results with the measurements, the regular seismic network managed by the KGHM mines it was found that these problems concern only low- and medium-energy events with a source located at a large distance from the measurement sites. For high-energy tremors with energy greater than 1x10$^6$ J at a distance of up to approximately 5 km, the inherent noise level of the ADIS16470 accelerometer should not negatively affect the measurement results.
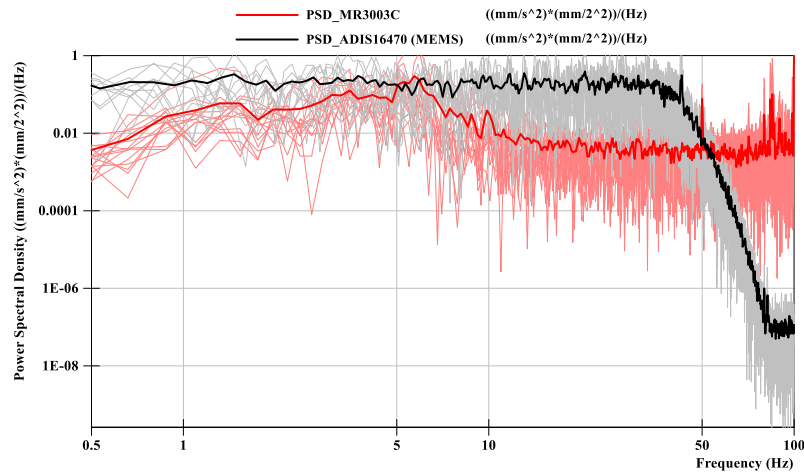
Fig. 10. Comparison of PSD distribution curves for noise recorded with the MEMS IMU ADIS16470 accelerometer (black) and a classic type accelerometer (red)

## 4.3. Recording rate unification for direct correlation calculations

Thanks to the use of the subspline method and the unification of the number of points in individual waveforms, it was also possible to calculate correlation coefficients for full seismic signal corresponding to individual seismic events. In the initial assumptions of this research, it was assumed that records from different measurement systems may differ significantly in the time domain due to different amplitude-frequency characteristics of used measuring devices. Therefore, it was proposed that the correlation coefficients between individual records should be determined based on the envelopes of seismic signals. However, it turned out that the raw signals recorded using a MEMS-IMU accelerometer and a classic accelerometer are so similar that it is possible to compare the raw signals directly with each other using the correlation matrix method to measure the degree of matching of the recorded signals. The calculation results for all 3 seismic components and for each recorded seismic event after filtering data in the range of 0.1-40 Hz are presented in Table 4. The waveform correlation has been computed for the time windows presented in figures 10-17.

Table 4. Calculated correlation coefficients of signals recorded with the MEMS-IMU accelerometer and the classic accelerometer

| Date of event | Correlation coefficient for the full waveforms $r_{xy}$ | | |
| --- | --- | --- | --- |
| | X | Y | Z |
| 19/09/2023 | 0.842800 | 0.735258 | 0.894078 |
| 22/09/2023 | 0.730907 | 0.633919 | 0.859396 |
| 28/09/2023 | 0.691446 | 0.624487 | 0.693733 |
| 12/10/2023 | 0.834049 | 0.679523 | 0.935465 |
| 13/10/2023 | 0.929384 | 0.804275 | 0.923567 |
| 17/10/2023 | 0.708869 | 0.684197 | 0.870140 |
| 17/11/2023 | 0.837859 | 0.919454 | 0.824089 |
| 18/11/2023 | 0.795800 | 0.933120 | 0.757327 |

The calculated correlation coefficients are in the range of 0.6245-0.9355, depending on the event and the measurement component. In general, the interpretation of the correlation coefficient is strictly dependent on the field of science in which it is used, however, as Hinkle et al. [19] point out, the values

obtained as a result of the analysis correspond to a strong (0.6-0.79) and very strong correlation (0.8-1), which clearly indicates the usefulness of low-cost MEMS-IMU (ADIS16470) in the field of conducting near-field seismicity measurements. Fig. 11-18 presents a graphical comparison of all recorded seismic waveforms. All three components from both accelerometers have a synchronized time to simplify the comparison of results.
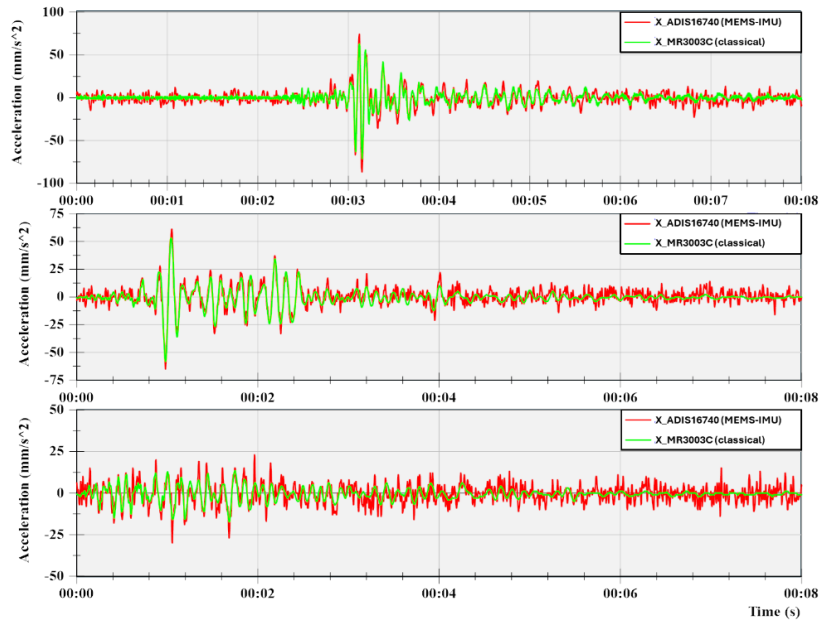


Fig. 11. Comparison of seismic waveforms recorded with the MEMS-IMU accelerometer (red) and the classic accelerometer (green) on September 19, 2023 for the X (top), Y (middle), and Z (bottom) components
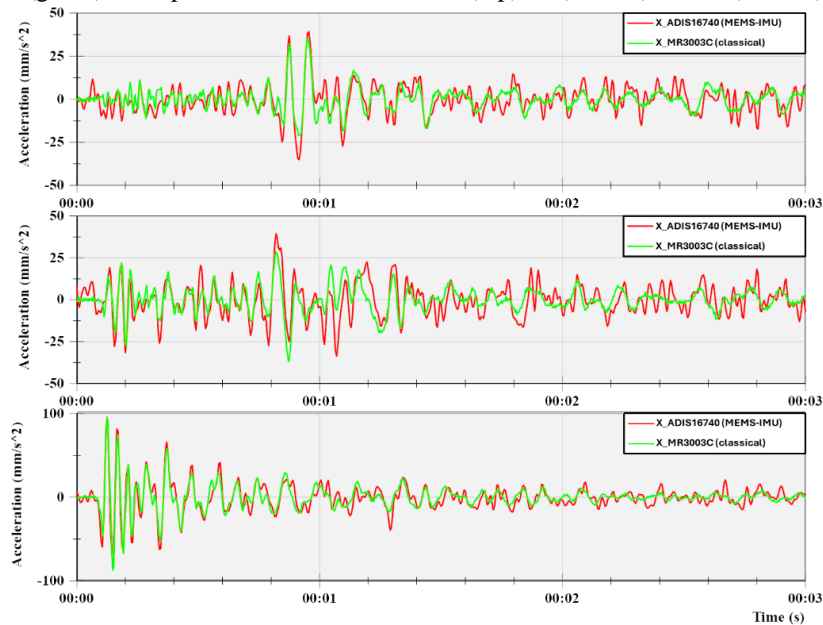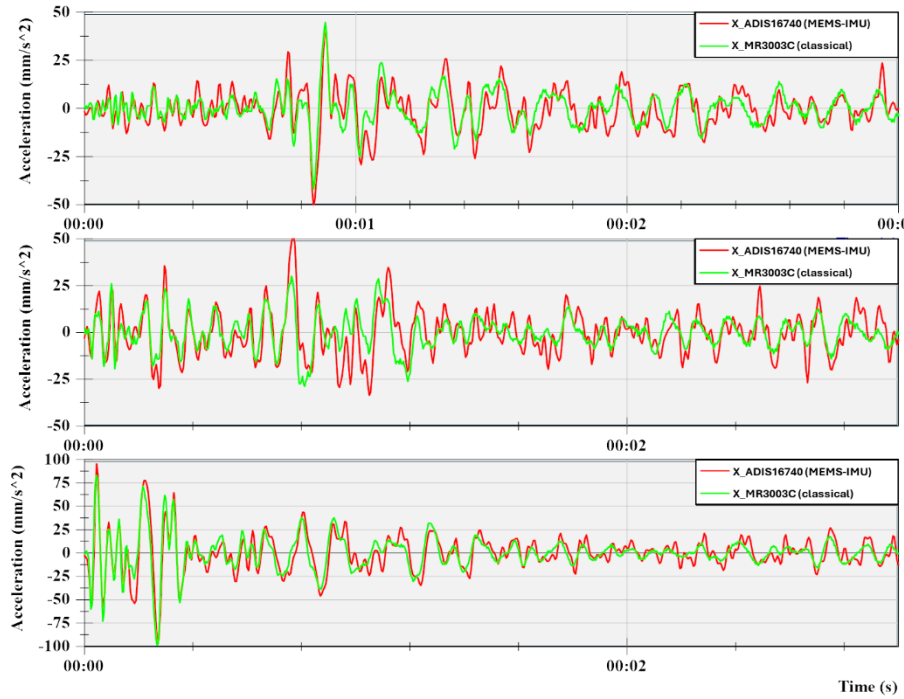


Fig. 12. Comparison of seismic waveforms recorded with the MEMS-IMU accelerometer (red) and the classic accelerometer (green) on September 22, 2023 for the X (top), Y (middle), and Z (bottom) components

Fig. 13. Comparison of seismic waveforms recorded with the MEMS-IMU accelerometer (red) and the classic accelerometer (green) on September 28, 2023 for the X (top), Y (middle), and Z (bottom) components
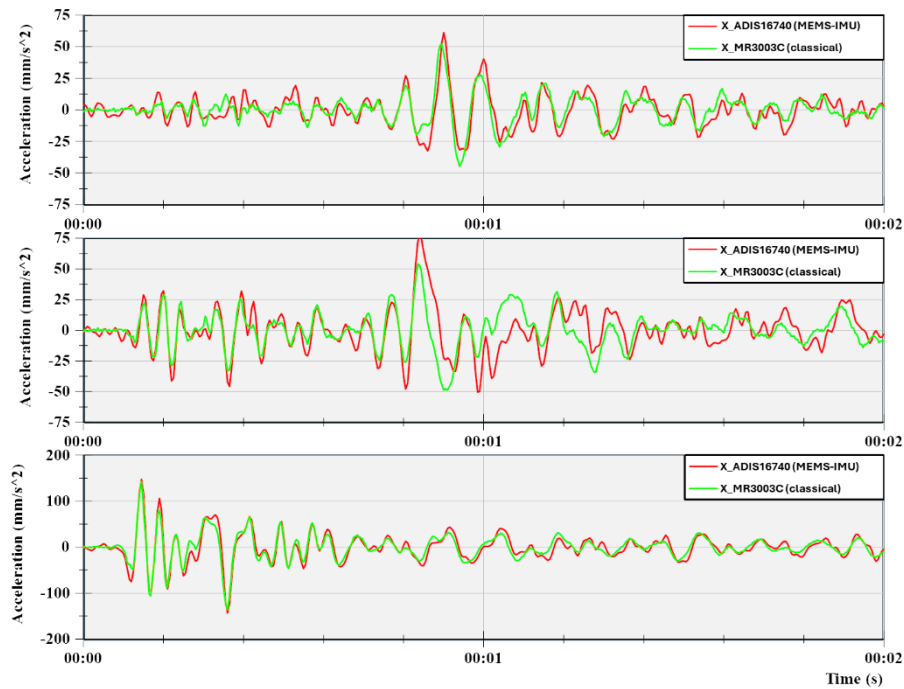


Fig. 14. Comparison of seismic waveforms recorded with the MEMS-IMU accelerometer (red) and the classic accelerometer (green) on 12/10/2023 for the X (top), Y (middle) and Z (bottom) components
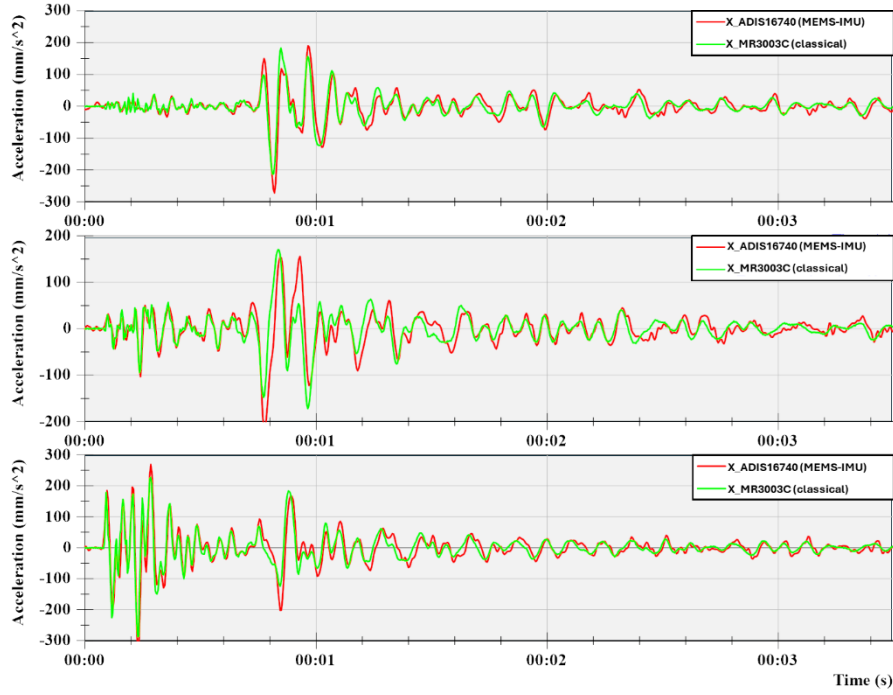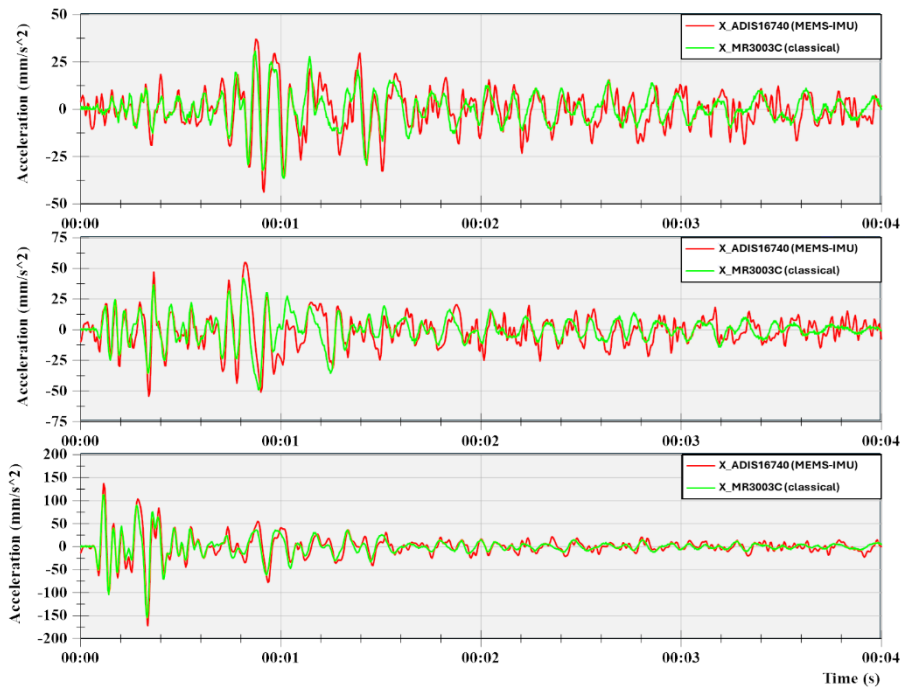
Fig. 15. Comparison of seismic waveforms recorded with the MEMS-IMU accelerometer (red) and the classic accelerometer (green) on 13/10/2023 for the X (top), Y (middle) and Z (bottom) components



Fig. 16. Comparison of seismic waveforms recorded with the MEMS-IMU accelerometer (red) and the classic accelerometer (green) on 17/10/2023 for the X (top), Y (middle) and Z (bottom) components
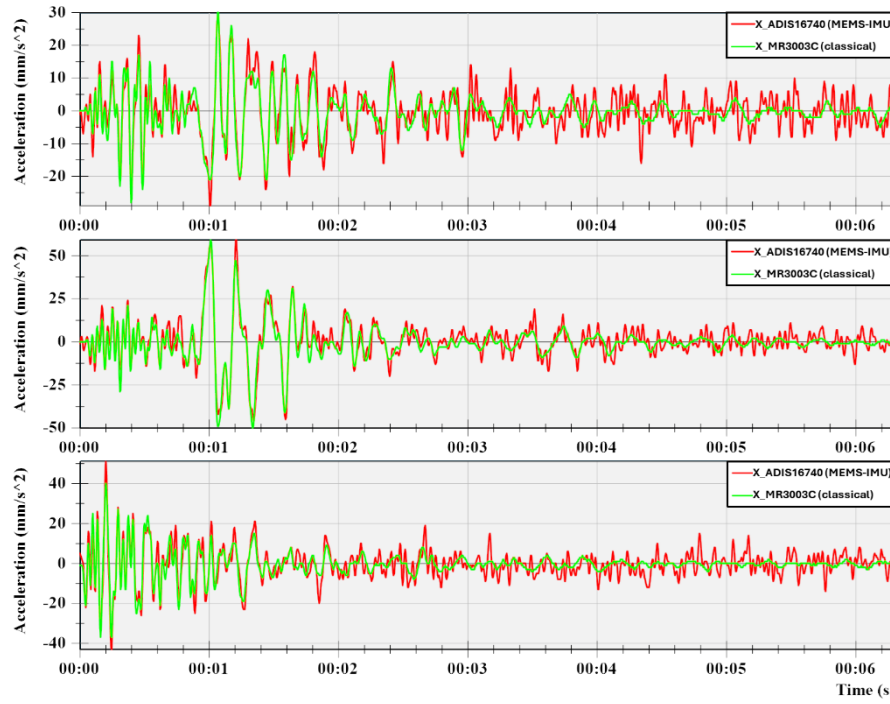
Fig. 17. Comparison of seismic waveforms recorded with the MEMS-IMU accelerometer (red) and the classic accelerometer (green) on November 17, 2023 for the X (top), Y (middle), and Z (bottom) components
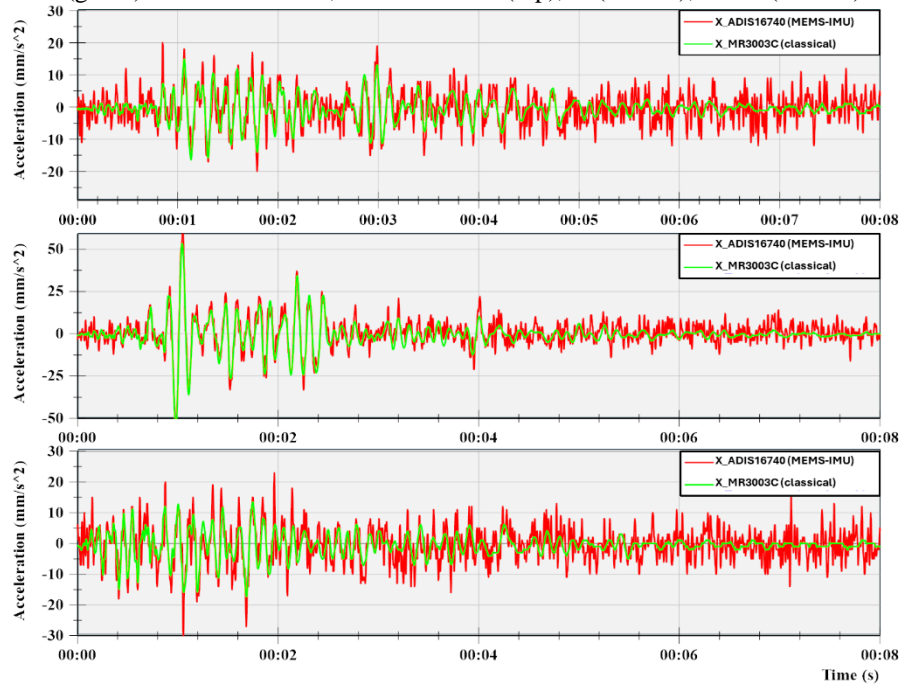


Fig. 18. Comparison of seismic waveforms recorded with the MEMS-IMU accelerometer (red) and the classic accelerometer (green) on November 18, 2023 for the X (top), Y (middle), and Z (bottom) components

Analyzing Figures 11-18, it can be observed that despite the overlapping trends, the signals recorded with the classic accelerometer are characterized by greater smoothness. This situation results from the fact that the ADIS16740 have significantly higher frequency content which is especially visible in the parts of the signal representing ambient noise (e.g. the final part of the signal in Fig. 17). This leads to conclusions analogous to those drawn from the comparison of PSD curves in Section 4.2. Additionally, for the complete data set for individual X, Y, and Z components, population and scatter plots were prepared, which is the basis for the analysis of discrepancies for individual amplitude ranges. The results are presented in Fig. 19, 20, and 21.
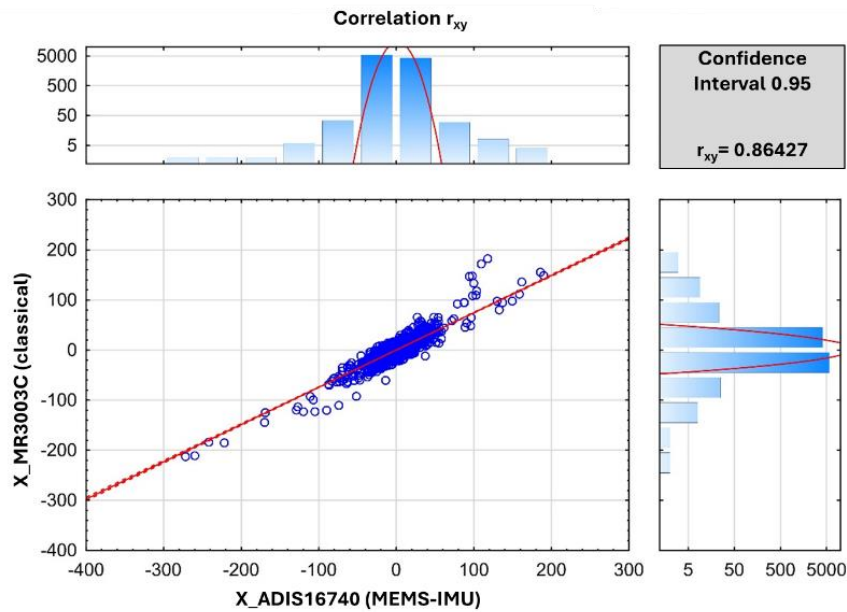
Fig. 19. Scatterplot and population for data recorded in the direction of the X component
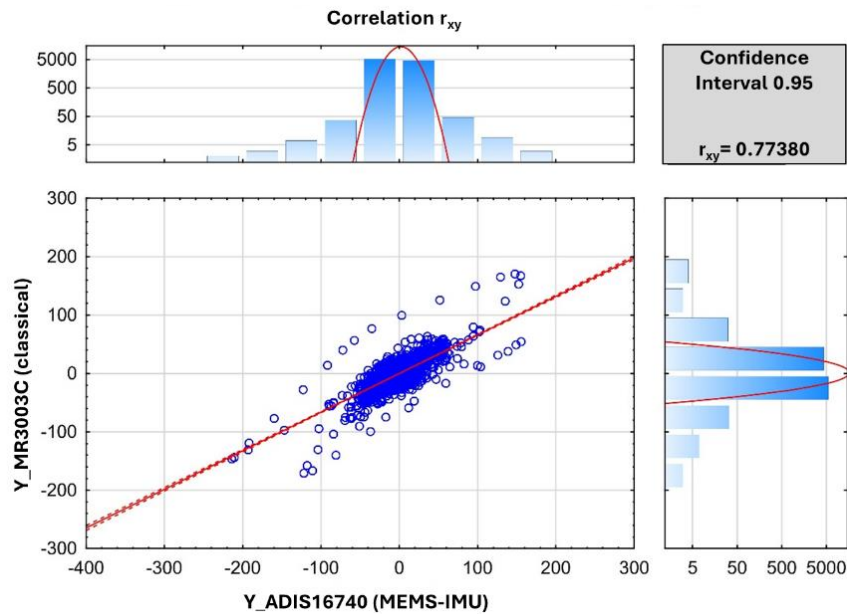
Fig. 20. Scatterplot and population for data recorded in the direction of the Y component
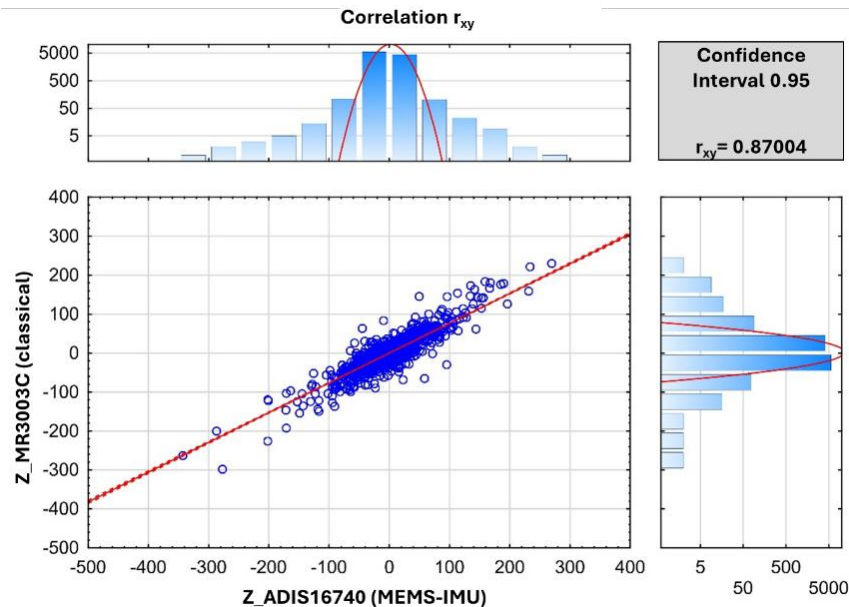
Fig. 21. Scatterplot and population for data recorded in the Z component direction

As results from the analysis, the correlation of the records for all three components X, Y and Z is 0.86, 0.77 and 0.87, respectively, which indicates a very high degree of matching of data from different types of accelerometers. Analyzing the scatterplots, one can observe a good correlation between the data from the MEMS-IMU accelerometer and the classic accelerometer in the full range of recorded values. The largest percentage deviations between individual records were observed in the case of low amplitudes, which is related to the higher level of self-noise generated by the MEMS-IMU accelerometer (ADIS16470). Nevertheless, the results are still similar enough to clearly confirm the applicability of MEMS-IMU accelerometers in the scope of surface measurements of seismic activity induced by mining activities.

## 5. CONCLUSIONS

Within this paper comparative verification of the records obtained using a low-cost MEMS-IMU accelerometer with a classic solution was presented, in order to, determine the usefulness of novel cost-effective technology for the purposes of mining seismicity monitoring. Comparison has been performed in terms of frequency and vibration amplitude distribution. As can be concluded, MEMS-IMU accelerometers, despite a slightly higher level of their self-noise, are characterized by high reliability of results, and the obtained vibration records correlate well with the waveforms recorded on a classic, calibrated measuring device. Of course, the devices also have their limitations. The relatively high level of self-noise translates into the lower usefulness of MEMS-IMU accelerometers in terms of locating and analysing the source of far-field tremors based on the differences in the arrival times of P and S waves. With the increase of distance between the source of the tremor and the measuring device, the high level of noise may cause some difficulties in determining the entry time of the P wave. On the other hand, this problem could be eliminated by increasing the density of the measurement network coverage. Such a solution seems to be possible considering the significant reduction in the costs of network development

and maintenance using innovative technologies. In terms of the dynamics of the device, frequency characteristics and recording parameters, MEMS-IMU accelerometers do not differ significantly from the parameters of devices currently used in the LGCB area. This is an important conclusion from the point of view of further development of monitoring systems in mining areas because the considered low-cost accelerometers are characterized by a unit price several dozen times lower than classic seismic systems.

One may notice that this paper focuses on the identification of high-energy tremor parameters. The issue of determining the detection threshold of the MEMS-based system is an element that will be analyzed in the near future. Considering the need to develop appropriate data processing algorithms to accurately determine the P-wave and S-wave arrival times, it was assumed that it is necessary to enlarge the low-energy events database to increase statistical population of results and define the applicability of the proposed solution to detect vibrations induced by tremors with energy in range of $1.0 \times 10^3$ J- $1.0 \times 10^4$ J.

Moreover, further studies will be aimed at determining the applicability of MEMS-IMU devices in underground conditions and at attempts to build a seismic network based solely on this type of devices. The efficiency and capacity of the network will once again be assessed using results from a regular seismic network used in the LGCB area.

## ADDITIONAL INFORMATION

## REFERENCES

1. Cieślik, J, Burtan, Z, Chlebowski, D and Zorychta, A 2017. Geomechanical analysis of location and conditions for mining-induced tremors in LGOM copper mines. *Journal of Sustainable Mining*, **16(3)**, 94–103. doi: 10.1016/j.jsm.2017.10.002
2. Fuławka, K, Pytel, W and Pałac-Walko, B 2020. Near-Field Measurement of Six Degrees of Freedom Mining-Induced Tremors in Lower Silesian Copper Basin. *Sensors,* **20(23)**, 6801. doi: 10.3390/s20236801
3. Das, J, Balasubramaniam, V, Goverdhan, K and Ganapathy, G 2016. *Overview of seismic monitoring and assessment of seismic hazard based on a decade of seismic events*. Proceedings of the conference on Recent Advances in Rock Engineering (RARE 2016), Atlantis Press, November 2016. https://doi.org/10.2991/rare-16.2016.90
4. Pytel, W, Fuławka, K, Pałac-Walko, B, Mertuszka, P, Kisiel, J, Jalas, P and Shekov, V 2020. Universal approach for risk identification and evaluation in underground facilities. *Mining Scince*, **27**, 165–181. doi: 10.37190/msc202712
5. Li, H, Cao, A, Gong, S, Wang, C and Zhang, R 2022. Evolution characteristics of seismic detection probability in underground mines and its application for assessing seismic risks—a case study. *Sensors*, **22(10)**, 3682. https://doi.org/10.3390/s22103682
6. Mendecki, AJ (Ed.). 1996. *Seismic Monitoring in Mines*. Dordrecht: Springer Netherlands. doi: 10.1007/978-94-009-1539-8

7.  Riemer, K, and Durrheim, R 2012. Mining seismicity in the witwatersrand basin: monitoring, mechanisms and mitigation strategies in perspective. *Journal of Rock Mechanics and Geotechnical Engineering*, **4(3)**, 228-249. https://doi.org/10.3724/sp.j.1235.2012.00228

8.  Trojanowski, J, Plesiewicz, B and Wiszniowski, J 2015. Seismic Monitoring of Poland–Description and Results of Temporary Seismic Project with Mobile Seismic Network. *Acta Geophysica*, **63(1)**, 17–44. doi: 10.2478/s11600-014-0255-0

9.  Fuławka, K, Mertuszka, P, Szumny, M, Stolecki, L, and Szczerbiński, K 2022. Application of MEMS-Based Accelerometers for Near-Field Monitoring of Blasting-Induced Seismicity. *Minerals*, **12(5)**, 533. doi: 10.3390/min12050533

10. Esposito, M, Marzorati, S, Belli, A, Ladina, C, Palma, L, Calamita, C and Pierleoni, P 2024. Low-cost MEMS accelerometers for earthquake early warning systems: A dataset collected during seismic events in central Italy. *Data in Brief*, **53**, 110174. doi: 10.1016/j.dib.2024.110174

11. Li, Z 2021. Recent advances in earthquake monitoring I: Ongoing revolution of seismic instrumentation. *Earthquake Science*, **34(2)**, 177–188. doi: 10.29382/eqs-2021-0011

12. Li Z. 2021. Recent advances in earthquake monitoring II: Emergence of next-generation intelligent systems. *Earthquake Science*, **34(6)**: 531–540,. DOI:  10.29382/eqs-2021-0054

13. KGHM Polska Miedź S.A. website: www.kghm.com, accessed on 9/2024.

14. EPOS TCS AH, website: https://episodesplatform.eu, accessed on 9/2024

15. Milczarek, W, Kopeć, A, Głąbicki, D and Bugajska, N 2021, Induced Seismic Events—Distribution of Ground Surface Displacements Based on InSAR Methods and Mogi and Yang Models. *Remote Sens*. **13**, 1451. https://doi.org/10.3390/rs13081451

16. McNamara, DE, Hutt, CR, Gee, LS, Benz, HM and Buland, RP 2009. A Method to Establish Seismic Noise Baselines for Automated Station Assessment. *Seismological Research Letters,* **80(4)**, 628–637. doi: 10.1785/gssrl.80.4.628

17. Jana, N, Singh, C, Biswas, R, Grewal, N and Singh, A 2017. Seismic noise analysis of broadband stations in the Eastern Ghat Mobile Belt of India using power spectral density. *Geomatics, Natural Hazards and Risk*, **8(2)**, 1622–1630. doi: 10.1080/19475705.2017.1365777

18. Akima, H 1970. A new method of interpolation and smooth curve fitting based on local procedures. *Journal of the ACM*. **17** 589–602. Archived (PDF) from the original on 2020-12-18. Retrieved 2020-12-18

19. Hinkle DE, Wiersma W and Jurs SG. Applied Statistics for the Behavioral Sciences. 5th ed. Boston: Houghton Mifflin; 2003.